

WERE PROGENITORS OF LOCAL L^* GALAXIES $\text{Ly}\alpha$ EMITTERS AT HIGH REDSHIFT?

HIDENOBU YAJIMA^{1,2}, YUEXING LI^{1,2}, QIRONG ZHU^{1,2}, TOM ABEL³, CARYL GRONWALL^{1,2}, ROBIN CIARDULLO^{1,2}

¹Department of Astronomy & Astrophysics, The Pennsylvania State University, 525 Davey Lab, University Park, PA 16802, USA

²Institute for Gravitation and the Cosmos, The Pennsylvania State University, University Park, PA 16802 and

³Kavli Institute for Particle Astrophysics and Cosmology, SLAC National Accelerator Laboratory, Stanford University, 2575 Sand Hill Road, Menlo Park, CA 94025, USA

Draft version November 1, 2018

ABSTRACT

The $\text{Ly}\alpha$ emission has been observed from galaxies over a redshift span $z \sim 0 - 8.6$. However, the evolution of high-redshift $\text{Ly}\alpha$ emitters (LAEs), and the link between these populations and local galaxies, remain poorly understood. Here, we investigate the $\text{Ly}\alpha$ properties of progenitors of a local L^* galaxy by combining cosmological hydrodynamic simulations with three-dimensional radiative transfer calculations using the new ART² code. We find that the main progenitor (the most massive one) of a Milky Way-like galaxy has a number of $\text{Ly}\alpha$ properties close to those of observed LAEs at $z \sim 2 - 6$, but most of the fainter ones appear to fall below the detection limits of current surveys. The $\text{Ly}\alpha$ photon escape fraction depends sensitively on a number of physical properties of the galaxy, such as mass, star formation rate, and metallicity, as well as galaxy morphology and orientation. Moreover, we find that high-redshift LAEs show blue-shifted $\text{Ly}\alpha$ line profiles characteristic of gas inflow, and that the $\text{Ly}\alpha$ emission by excitation cooling increases with redshift, and becomes dominant at $z \gtrsim 6$. Our results suggest that some observed LAEs at $z \sim 2 - 6$ with luminosity of $L_{\text{Ly}\alpha} \sim 10^{42-43} \text{ erg s}^{-1}$ may be similar to the main progenitor of the Milky Way at high redshift, and that they may evolve into present-day L^* galaxies.

Subject headings: radiative transfer – line: profiles – hydrodynamics – cosmology: computation – galaxies: evolution – galaxies: formation – galaxies: high-redshift

1. INTRODUCTION

The $\text{Ly}\alpha$ emission from young galaxies can be a powerful probe of the early universe (Partridge & Peebles 1967; Charlot & Fall 1993). Recent narrow-band deep imaging surveys using large-aperture telescopes have detected a large number of $\text{Ly}\alpha$ emitting galaxies, or $\text{Ly}\alpha$ emitters (LAEs), at redshifts $z \gtrsim 3$ (e.g., Hu & McMahon 1996; Cowie & Hu 1998; Steidel et al. 2000; Malhotra & Rhoads 2004; Taniguchi et al. 2005; Kashikawa et al. 2006; Shimasaku et al. 2006; Iye et al. 2006; Hu & Cowie 2006; Gronwall et al. 2007; Ouchi et al. 2008; Hu et al. 2010; Ouchi et al. 2010; Lehnert et al. 2010). By combining $\text{Ly}\alpha$ emission with broad-band continuum, multi-wavelength observations are beginning to address the physical properties of these high-redshift LAEs (e.g., Gawiser et al. 2006; Gronwall et al. 2007; Lai et al. 2007; Nilsson et al. 2007; Pirzkal et al. 2007; Lai et al. 2008; Ouchi et al. 2008; Pentericci et al. 2009; Ono et al. 2010a,b; Hayes et al. 2010; Finkelstein et al. 2011; Nilsson & Møller 2011; Acquaviva et al. 2011). It has been suggested that these objects are mostly compact, young galaxies with low metallicity. In addition, Ouchi et al. (2008) studied the evolution of equivalent widths (EWs) and the characteristic $L_{\text{Ly}\alpha}^*$ with redshift from $z \sim 3$ to $z \sim 6$, and found that the mean EW increased with redshift, while the $L_{\text{Ly}\alpha}^*$ did not change significantly. More recently, Ciardullo et al. (2011) studied the evolution of luminosity function (LF) and EW from $z = 2.1$ to 3.1 , and found that L_* increases from $10^{42.3} \text{ erg s}^{-1}$ at

$z = 2.1$ to $10^{43} \text{ erg s}^{-1}$ at $z = 3.1$. Blanc et al. (2011) studied the $\text{Ly}\alpha$ properties of LAEs in the redshift range $z = 1.9 - 3.8$ from the Hobby Eberly Telescope Dark Energy Experiment (HETDEX) Pilot Survey, and showed that the median $\text{Ly}\alpha$ escape fraction (f_{esc}) was $\sim 29\%$, and it does not evolve significantly with redshift. On the other hand, Hayes et al. (2011) suggested that f_{esc} monotonically increases between redshift 0 and 6, which implies that high- z galaxies tend to be LAEs.

While high-redshift LAEs have been studied with large samples in the redshift range of $z \sim 2.2 - 6.6$, there is only a limited number of observations on LAEs at $z \lesssim 1$. Some local star-forming galaxies have been studied by various wavelengths and show a complex structure of $\text{Ly}\alpha$ and UV continuum (Hayes et al. 2007; Östlin et al. 2009). Atek et al. (2009) showed that the f_{esc} of local LAEs have a large dispersion, ranging from ~ 3 to 100% . In addition, Deharveng et al. (2008) studied a sample of 96 local LAEs at $z = 0.2 - 0.35$ from UV space telescope *GALEX*, and found that these LAEs have similar EW distribution as those at $z = 3.1$. Recently, Cowie et al. (2010) have studied $z \sim 0.3$ LAEs with a larger sample, and showed that these LAEs are more compact, and have lower metallicity than UV-continuum selected galaxies at the same redshift. In addition, Finkelstein et al. (2009) suggested, from fitting of spectral energy distributions (SEDs), that low- z LAEs are significantly more massive and older galaxies than their high- z counterparts.

One of the important issues in galaxy evolution is how high-redshift LAEs evolve into galaxies in the local universe. Gawiser et al. (2007) suggested, from clustering analysis, that most $z = 3.1$ LAEs evolve to present-day galaxies of $\lesssim 2.5 L^*$, unlike other populations which

typically evolve into more massive galaxies. Moreover, Guaita et al. (2010) indicated that LAEs at $z = 2.1$ were building blocks of present-day L^* galaxies such as the Milky Way (MW).

However, the link between high-redshift LAEs and local galaxies, and the probability of these LAEs evolving into present-day L^* galaxies are not well constrained from observations. In order to address these questions, one may use the Milky Way as a local laboratory. Moreover, since Ly α emission has been detected from the most distant galaxies, understanding of the Ly α properties of the Milky Way progenitors will provide an important clue to the formation of early galaxies. To date, there are only a limited number of theoretical studies on this important issue (e.g., Salvadori et al. 2010; Dayal & Libeskind 2011). Both Salvadori et al. (2010) and Dayal & Libeskind (2011) focused on MW progenitors at $z \sim 6$ constructed from semi-analytical merger trees and a cosmological smoothed particle hydrodynamics (SPH) simulation, respectively. They both used the same analytical prescription of Ly α emission in which the intrinsic Ly α luminosity scales linearly with the star formation rate (Dayal et al. 2008). However, because the Ly α properties depend sensitively on a number of factors, such as the scattering and propagation of the photons in the inhomogeneous medium, the dust content of the gas, the ionization structure, the UV continuum, and the photon escape fraction. Such a complicated process can only be probed by comprehensive Ly α radiative transfer calculations combined with realistic simulation of galaxy formation. As we will show in this work, our detailed Ly α modeling on a high-resolution cosmological simulation produce a number of Ly α properties such as the luminosity functions at different redshifts in good agreement with observations. Moreover, in order to investigate the evolution of LAEs, we need to study the progenitors of the MW at different redshifts systematically, not just at a specific time.

In this paper, we investigate the Ly α properties of MW progenitors over a wide redshift range of $z \sim 0 - 10$, by combing cosmological SPH simulation of a MW-like galaxy from Zhu et al. (in preparation) with 3D RT calculations using the newly improved ART² code by Yajima et al. (2011). Our hydrodynamic simulation includes important physics of both dark and baryonic matter, and has high resolutions to track the formation history of the MW. Our RT calculations include both Ly α resonant scattering and continuum emission, and are done on an adaptive-mesh refinement grid, which covers a large dynamical range and resolves the small-scale structures in high-density region. Interstellar dust is also taken into account to accurately estimate the f_{esc} of Ly α photons and UV continuum, and the EWs.

The paper is organized as follows. We describe our cosmological simulation in §2, and the RT calculations in §3. In §4, we present results of the Ly α properties of MW progenitors from redshift 10 to 0, which include the Ly α surface brightness, Ly α luminosity, f_{esc} , EW and line profile. In §5, we discuss the dependence of f_{esc} on physical properties, LAE fraction in our galaxy sample, Ly α escaping angle and the contribution from excitation cooling to Ly α emissivity, and we summarize in §6.

2. GALAXY MODEL

The cosmological simulation presented here follows the formation and evolution of a Milky Way-size galaxy and its substructures, as described in detail in Zhu et al. (in preparation). The simulation includes dark matter, gas dynamics, star formation, black hole growth, and feedback processes. The initial condition is originally from the Aquarius Project (Springel et al. 2008), which produced the largest ever particle simulation of a Milky Way-sized dark matter halo. The hydrodynamical initial condition is reconstructed from the original collisionless one by splitting each original particle into a dark matter and gas particle pair, as adopted from Wadepuhl & Springel (2011).

The whole simulation falls in a periodic box of $100 h^{-1}\text{Mpc}$ on each side with a zoom-in region of a size $5 \times 5 \times 5 h^{-3}\text{Mpc}^3$. The spatial resolution is $\sim 250 h^{-1}\text{pc}$ in the zoom-in region. The mass resolution of this zoom-in region is $1.8 \times 10^6 h^{-1}M_{\odot}$ for dark matter particles, $3 \times 10^5 h^{-1}M_{\odot}$ for gas, and $1.5 \times 10^5 h^{-1}M_{\odot}$ for star particles. The cosmological parameters used in the simulation are $\Omega_m = 0.25$, $\Omega_{\Lambda} = 0.75$, $\sigma_8 = 0.9$ and $h = 0.73$, consistent with the five-year results of the WMAP (Komatsu et al. 2009). The simulation evolves from $z = 127$ to $z = 0$.

The simulation was performed using the parallel, N-body/SPH code GADGET-3, which is an improved version of that described in Springel et al. (2001); Springel (2005). For the computation of gravitational forces, the code uses the “TreePM” method (Xu 1995) that combines a “tree” algorithm (Barnes & Hut 1986) for short-range forces and a Fourier transform particle-mesh method (Hockney & Eastwood 1981) for long-range forces. GADGET implements the entropy-conserving formulation of SPH (Springel & Hernquist 2002) with adaptive particle smoothing, as in Hernquist & Katz (1989). Radiative cooling and heating processes are calculated assuming collisional ionization equilibrium (Katz et al. 1996; Davé et al. 1999). Star formation is modeled in a multi-phase ISM, with a rate that follows the Schmidt-Kennicutt Law (Schmidt 1959; Kennicutt 1998). Feedback from supernovae is captured through a multi-phase model of the ISM by an effective equation of state for star-forming gas (Springel & Hernquist 2003). The UV background model of Haardt & Madau (1996) is used.

Black hole growth and feedback are also included in our simulation based on the model of Springel et al. (2005b); Di Matteo et al. (2005), where black holes are represented by collisionless “sink” particles that interact gravitationally with other components and accrete gas from their surroundings. The accretion rate is estimated from the local gas density and sound speed using a spherical Bondi-Hoyle (Bondi 1952; Bondi & Hoyle 1944; Hoyle & Lyttleton 1941) model that is limited by the Eddington rate. Feedback from black hole accretion is modeled as thermal energy, $\sim 5\%$ of the radiation, injected into surrounding gas isotropically, as described in Springel et al. (2005b) and Di Matteo et al. (2005). This feedback scheme self-regulates the growth of the black hole and has been demonstrated to successfully reproduce many observed properties of local elliptical galaxies (e.g., Springel et al. 2005a; Hopkins et al. 2006) and the most distant quasars at $z \sim 6$ (Li et al. 2007). We fol-

low the black hole seeding scheme of Li et al. (2007) and Di Matteo et al. (2008) in the simulation: a seed black hole of mass $M_{\text{BH}} = 10^5 h^{-1} M_{\odot}$ was planted in the gravitational potential minimum of each new halo identified by the friends-of-friends (FOF) group finding algorithms with a total mass greater than $10^{10} h^{-1} M_{\odot}$.

The galaxies in each snapshot above redshift 0 are building blocks of the MW, a present-day L^* galaxy. We therefore define them as “progenitors” of the MW, and the most massive progenitor at any given timestep as the “main progenitor”. In this paper, we explore the Ly α properties of ~ 60 most massive progenitors of each snapshot for 15 snapshots in the redshift range $z = 0 - 10.2$, which gives a total sample of 941 galaxies.

3. RADIATIVE TRANSFER

The RT calculations are done using the 3D Monte Carlo RT code, All-wavelength Radiative Transfer with Adaptive Refinement Tree (ART²), as recently developed by Yajima et al. (2011). ART² was improved over the original version of Li et al. (2008), and features three essential modules: continuum emission from X-ray to radio, Ly α emission from both recombination and collisional excitation, and ionization of neutral hydrogen. The coupling of these three modules, together with an adaptive refinement grid, enables a self-consistent and accurate calculation of the Ly α properties, which depend strongly on the UV continuum, ionization structure, and dust content of the object. Moreover, it efficiently produces multi-wavelength properties, such as the spectral energy distribution and images, for direct comparison with multi-band observations. The detailed implementations of the ART² code are described in Li et al. (2008) and Yajima et al. (2011). Here we focus on the Ly α calculations and briefly outline the process.

The Ly α emission is generated by two major mechanisms: recombination of ionizing photons and collisional excitation of hydrogen gas. In the recombination process, we consider ionization of neutral hydrogen by ionizing radiation from stars, active galactic nucleus (AGN), and UV background (UVB), as well as by collisions by high-temperature gas. The ionized hydrogen atoms then recombine and create Ly α photons via the state transition $2P \rightarrow 1S$. The Ly α emissivity from the recombination is

$$\epsilon_{\alpha}^{\text{rec}} = f_{\alpha} \alpha_{\text{B}} h\nu_{\alpha} n_{\text{e}} n_{\text{HII}}, \quad (1)$$

where α_{B} is the case B recombination coefficient, and f_{α} is the average number of Ly α photons produced per case B recombination. Here we use α_{B} derived in Hui & Gnedin (1997). Since the temperature dependence of f_{α} is not strong, $f_{\alpha} = 0.68$ is assumed everywhere (Osterbrock & Ferland 2006). The product $h\nu_{\alpha}$ is the energy of a Ly α photon, 10.2 eV.

In the process of collisional excitation, high temperature electrons can excite the quantum state of hydrogen gas by the collision. Due to the large Einstein A coefficient, the hydrogen gas can occur de-excitation with the Ly α emission. The Ly α emissivity by the collisional excitation is estimated by

$$\epsilon_{\alpha}^{\text{coll}} = C_{\text{Ly}\alpha} n_{\text{e}} n_{\text{HI}}, \quad (2)$$

where $C_{\text{Ly}\alpha}$ is the collisional excitation coefficient, $C_{\text{Ly}\alpha} = 3.7 \times 10^{-17} \exp(-h\nu_{\alpha}/kT) T^{-1/2}$ ergs s⁻¹ cm³

(Osterbrock & Ferland 2006).

Once the ionization structure have been determined, we estimate the intrinsic Ly α emissivity in each cell by the sum of above Ly α emissivity, $\epsilon_{\alpha} = \epsilon_{\alpha}^{\text{rec}} + \epsilon_{\alpha}^{\text{coll}}$.

In RT calculations, dust extinction from the ISM is included. The dust content is estimated according to the gas content and metallicity in each cell, which are taken from the hydrodynamic simulation. The dust-to-gas ratio of the MW is used where the metallicity is of Solar abundance, and it is linearly interpolated for other metallicity. We use the stellar population synthesis model of GALAXEV (Bruzual & Charlot 2003) to produce intrinsic SEDs of stars for a grid of metallicity and age, and we use a simple, broken power law for the AGN (Li et al. 2008). A Salpeter (1955) initial mass function is used in our calculations.

In this work, we apply ART² to the 60 most massive progenitors of each snapshot for 15 snapshots at redshifts spanning $z = 0 - 10.2$. In our post-processing procedure, we first calculate the RT of ionizing photons ($\lambda \leq 912 \text{ \AA}$) and estimate the ionization fraction of the ISM. The resulting ionization structure is then used to run the Ly α RT to derive the emissivity, followed by the calculation of non-ionizing continuum photons ($\lambda > 912 \text{ \AA}$) in each cell. Our fiducial run is done with $N_{\text{ph}} = 10^5$ photon packets for each ionizing, Ly α , and non-ionizing components. Because the spatial resolution of the cosmological simulation is not adequate to resolve the multiple phase of the ISM, we assume a single-phase medium in each density grid. The highest refinement of the grid corresponds to a cell size comparable to the spatial resolution of 250 pc in comoving coordinate of the hydrodynamic simulation.

4. RESULTS

4.1. The Formation History of The Milky Way

Figure 1 shows the evolution of the MW galaxy from redshift $z=10$ to $z=0$ from the cosmological simulation. The gas follows the distribution of dark matter in filamentary structures, and stars form in high density regions along the filaments. The most massive galaxy resides in the intersection of the filaments, the highest density peak in the simulated volume where gas concentrates in the deep potential well. The MW galaxy is formed by gas accretion and merger of subhalos, it has the last major merger at redshift $z \sim 2$ (Zhu et al, in preparation).

Stars start to form at $z \sim 15$ by accretion of cold gas. As shown in Figure 2, the star formation rate (SFR) of the main progenitor reaches $\sim 10 M_{\odot} \text{ yr}^{-1}$ at $z \sim 10$, and it peaks at $\sim 58 M_{\odot} \text{ yr}^{-1}$ at $z = 5.2$, owing to merger of gas-rich protogalaxies. Galaxy interaction induces gravitational torques and shocks, which trigger global starburst. After that, the SFR generally decreases except a boosted bump at $z \sim 2$ when the last major merger takes place.

Shown also in Figure 2 are the SFRs of the top 60 progenitors at different redshifts. The median and total value of these SFRs gradually increase until it reaches the peak at $z \sim 3.5$, after which it decreases rapidly by over an order of magnitude. This evolution is in broad agreement with the observed cosmic star formation history (Hopkins & Beacom 2006), although the simulation box is somewhat small to discuss such a statistical property.

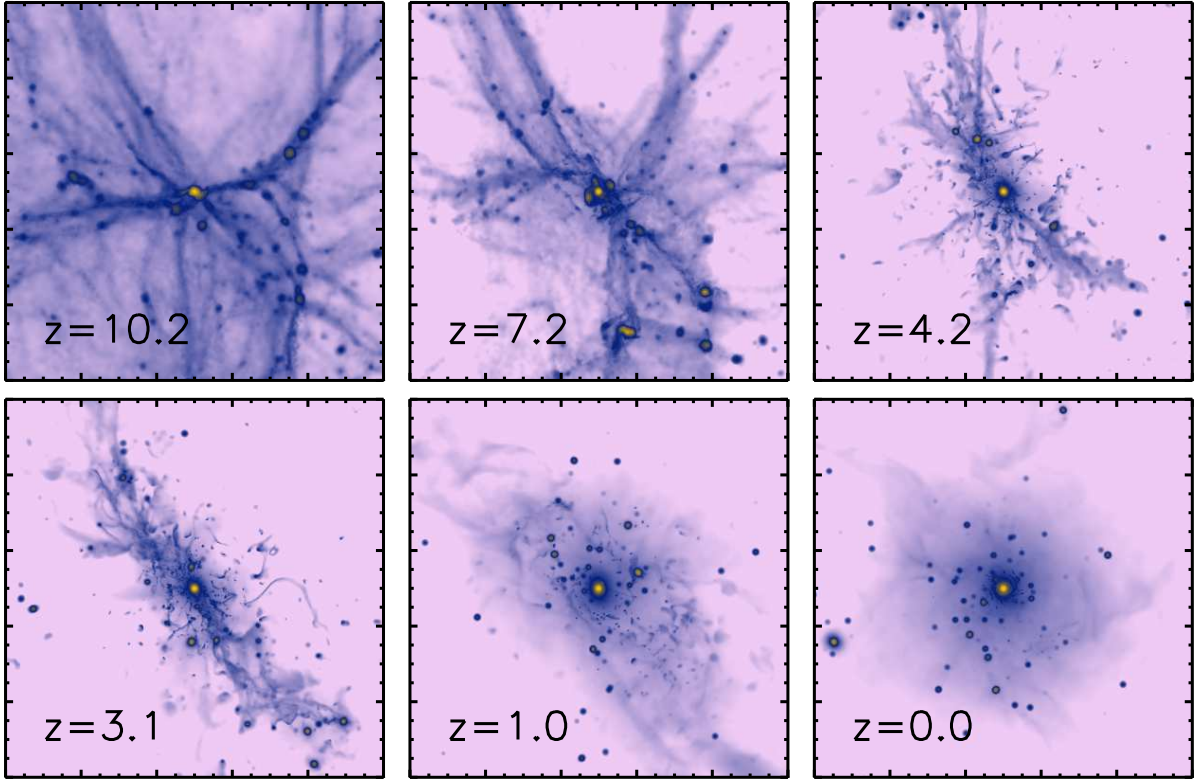


FIG. 1.— Evolution of the MW galaxy from redshift $z=10$ to $z=0$. The images are projected density of gas and stars. The box size is 1 Mpc in comoving scale. The gas follows the distribution of dark matter and shows filamentary structures. Stars and galaxies form in high density regions along the filaments.

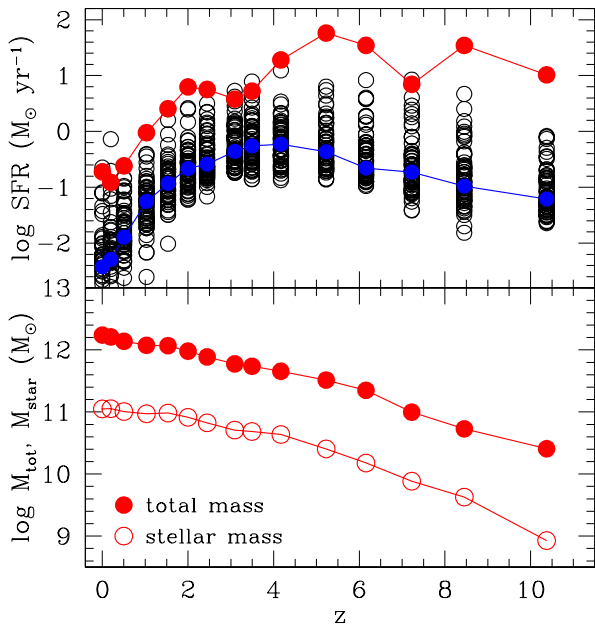


FIG. 2.— The growth history of the MW galaxy. Top panel: the individual star formation history of the most massive 60 progenitors at each redshift. Red filled circles represent the main progenitor (the most massive one), and the blue filled circles indicate the median value of our sample galaxies represented by black open circles. Bottom panel: the accumulated mass of the main progenitor at different redshift. Filled circle represents the total mass, while the open circle represents the stellar mass.

The star formation at high redshifts ($z \gtrsim 4$) is largely fueled by inflow of cold gas and mergers of gas-rich halos, while the rapid decline of SFR at $z \lesssim 2$ is mainly caused by feedback from stars and AGNs, and the depletion of cold gas.

The main progenitor has a total mass of $\sim 2.6 \times 10^{10} M_{\odot}$, and a stellar mass of $\sim 8.5 \times 10^8 M_{\odot}$ at $z \sim 10$. It evolved into a disk galaxy at $z = 0$ with a total mass of $1.6 \times 10^{12} M_{\odot}$ and stellar mass of $\sim 10^{11} M_{\odot}$, as observed in the MW galaxy.

4.2. Ly α Surface Brightness

Figure 3 shows the Ly α surface brightness of the MW galaxy at different redshifts, contrasted with distributions of gas and stars of the galaxy. To facilitate comparison with observations, we adopt an intensity threshold, $S_{\text{Ly}\alpha} = 10^{-18} \text{ ergs s}^{-1} \text{ cm}^{-2} \text{ arcsec}^{-2}$, from a recent survey of extended Ly α sources at $z \sim 3$ by Matsuda et al. (2011) to show the contours. The Ly α distribution appears to trace that of the gas. At $z \geq 7.2$, the galaxy is small and compact, and the Ly α emission is confined in the central high-density region. As the galaxy grows in mass and size, the Ly α emission becomes more extended. At $z = 4.2 - 3.1$, the gas structure is irregular due to infall along with filament of the main halo. At $z \sim 0.0$, the galaxy shows a disk geometry with spiral structures. Indeed, the Ly α map shows filamentary structures at high redshift, and spirals at $z \sim 0.0$. We note that some of the extended Ly α sources in the recent observations by Matsuda et al. (2011), which are called Ly α blobs, show filamentary structures. Our galaxy

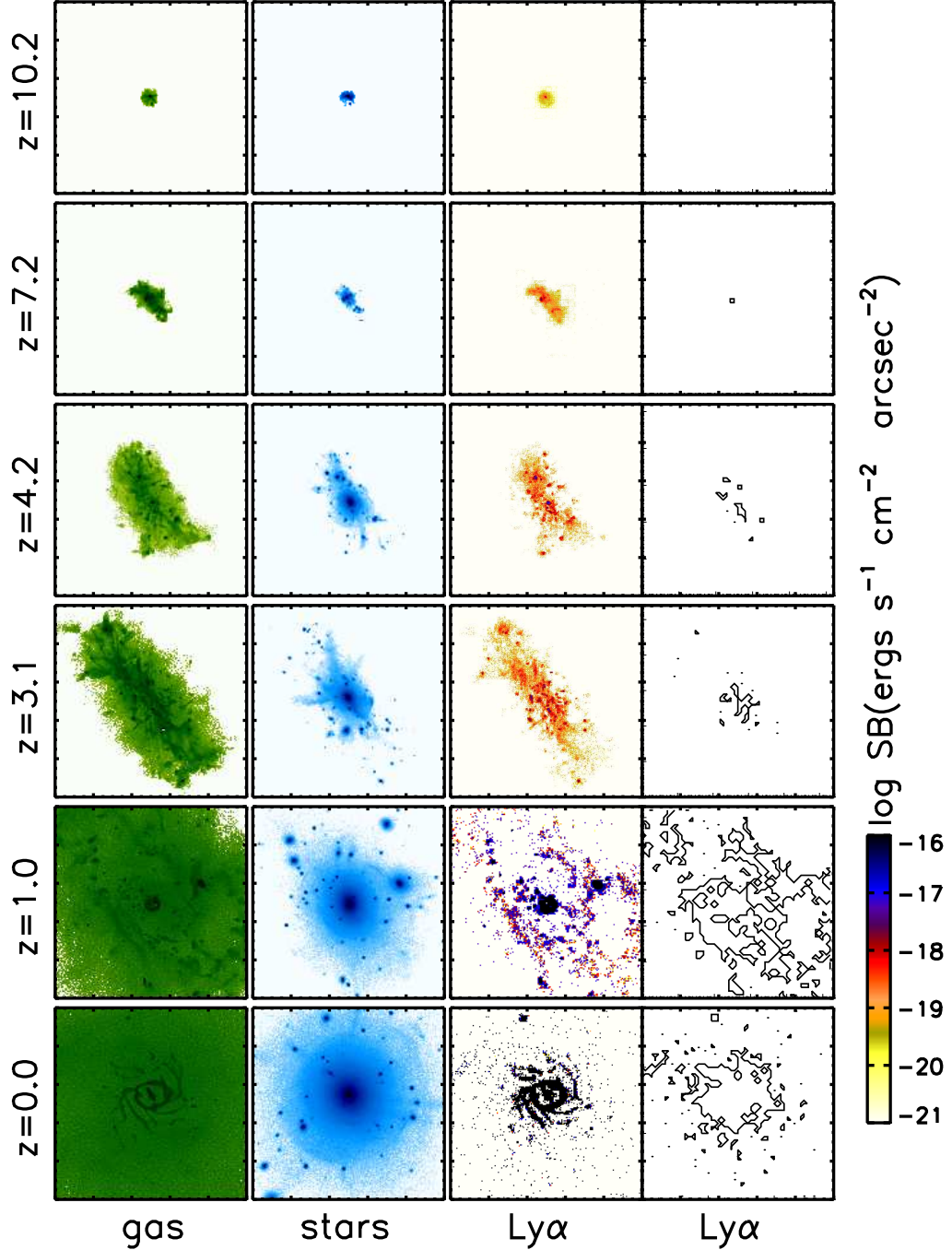


FIG. 3.— Evolution of the Ly α surface brightness of the MW galaxy with redshift. The first and second columns show the distribution of gas (in green) and stars (in blue) from the cosmological simulation, respectively. The third column shows the surface brightness of Ly α in log scale with units of $\text{ergs s}^{-1} \text{cm}^{-2} \text{arcsec}^{-2}$. The box size is 200 kpc in physical coordinates. Note the galaxy at $z = 0$ is artificially placed at $z = 0.1$ in order to obtain the luminosity distance. The right column shows the contour of Ly α surface brightness at the level of $10^{-18} \text{ ergs s}^{-1} \text{cm}^{-2} \text{arcsec}^{-2}$, similar to the threshold of recent observations of extended Ly α sources by Matsuda et al. (2011). The meshes are coarse grained to be 4 kpc in physical scale to make the smooth contours.

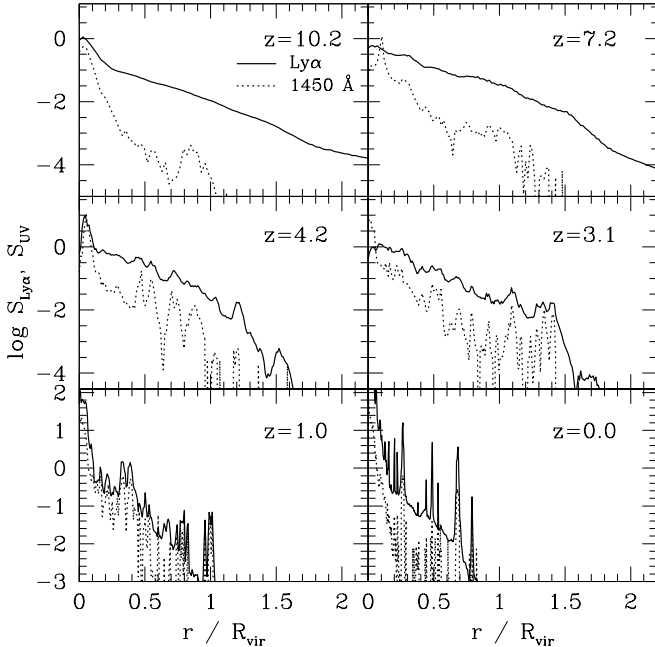


FIG. 4.— Radial distribution of the surface brightness of the MW galaxy at different redshift. The solid line shows the Ly α surface brightness in units of 10^{-18} ergs s^{-1} cm^{-2} arcsec $^{-2}$, while the dotted line shows the surface brightness of UV continuum at 1450 Å in rest frame in units of 10^{-31} ergs s^{-1} cm^{-2} Hz $^{-1}$ arcsec $^{-2}$. The surface brightness distribution is derived from the projected flux images in figure 3 by taking the mean surface brightness as a function of the distance.

at $z = 3.1$ has a Ly α distribution of ~ 50 kpc with a surface brightness above the observational threshold. However, the size is smaller than the observed giant Ly α blobs of $\gtrsim 100$ kpc. Such large blobs are probably produced by systems of $M_{\text{halo}} \gtrsim 10^{12} M_{\odot}$, more massive than our model. In addition, it was suggested that extended Ly α sources of $\gtrsim 40$ kpc become rare at $z < 1$ (Keel et al. 2009). Recent UV surveys detected Ly α from local star-forming galaxies at $z \lesssim 1$, which showed ~ 10 kpc Ly α distribution above the threshold of $S_{\text{Ly}\alpha} \sim 10^{-14}$ ergs s^{-1} cm^{-2} arcsec $^{-2}$ (Hayes et al. 2007; Östlin et al. 2009). With such a detection sensitivity, our model galaxies at $z \lesssim 1$ show the size of $\lesssim 20$ kpc, in broad agreement with observations.

To examine the difference in distribution between stars and Ly α emission more quantitatively, Figure 4 shows the surface brightness of UV continuum, which traces young stars, and Ly α as a function of the distance from galaxy center at different time. At high redshift ($z \gtrsim 5$), the Ly α distributes more extendedly than the stars, as the UV continuum decreases steeply around the virial radius, but at $z < 3$, both emissions appear to have similar radial distribution. Such a transition is mainly due to the difference in Ly α production at different epochs. The Ly α emission is dominated by collisional excitation, which depends strongly on the gas density, at $z \gtrsim 5$. At a later time, Ly α from recombination of ionized gas by stellar radiation becomes more important, so Ly α emission follows that of stars.

It was shown by Cowie et al. (2011) that nearby LAEs ($z \lesssim 1.0$) have a variety of morphologies, some are disk-

while others are mostly compact galaxies. Galaxy morphology is closely tied to galaxy formation and evolution, and it is related to the galaxy mass. As demonstrated in Figure 5, which shows a sample of four galaxies of different masses at $z = 0.2$, the Ly α morphology changes with galaxy mass. In galaxies with lower mass ($M_{\text{tot}} \lesssim 10^{11} M_{\odot}$), the Ly α luminosity is low ($L_{\text{Ly}\alpha} \lesssim 10^{42}$ erg s^{-1}), the Ly α morphology is highly compact. At higher mass ($M_{\text{tot}} \gtrsim 10^{11} M_{\odot}$), the Ly α luminosity is high ($L_{\text{Ly}\alpha} \gtrsim 10^{42}$ erg s^{-1}), Ly α morphology shows disk and spiral structures. This plot suggests that the various morphologies observed in low-redshift LAEs may reflect a wide range of galaxy mass in the sample.

We note that in Figure 4, the azimuthally averaged surface brightness at $z \gtrsim 3$ is somewhat fainter than the detection threshold of recent narrow-band surveys, $\sim 10^{-18}$ ergs s^{-1} cm^{-2} arcsec $^{-2}$ (Ouchi et al. 2008). However, since the local Ly α distribution is inhomogeneous and anisotropic, as shown in Figure 3, so bright regions with flux above the threshold may be detectable by such surveys.

The detectability of these galaxies depends strongly on the sensitivity of the surveys. In the present work, unless noted otherwise, the Ly α luminosity is computed by collecting all escaped photons without a flux limit. If a detection limit of a given instrument is imposed, the luminosity of individual galaxies, in particular that of the faint ones, may be reduced significantly, as suggested by Zheng et al. (2010).

4.3. Evolution of Spectral Energy Distribution

The corresponding multi-wavelength SEDs of the galaxy sample in Figure 3 are shown in Figure 6. The shape of the SED changes significantly from $z = 10.2$ to $z = 0$, as a result of changes in radiation source and environment, since the radiation from stars, absorption of ionizing photons by gas and dust, and re-emission by the dust evolve dynamically with time. The Ly α line appears to be strong in all cases. The deep decline of Lyman continuum ($l \leq 912$ Å) at high redshifts ($z \gtrsim 7$) is caused by strong absorption of ionizing photons by the dense gas. Galaxies at lower redshift have a higher floor of continuum emission from stars and accreting BHs, a higher ionization fraction of the gas, and a higher infrared bump owing to increasing amount of dust and absorption. Moreover, due to the effect of negative k-correction, the flux at observed frame $\lambda \gtrsim 500$ μm stays close in different redshifts.

Our calculations show that the main progenitor has a flux of $f_{\nu} = 0.057$ mJy at $z \sim 6$ and 0.02 mJy at $z \sim 8.5$ at 850 μm in observed frame. The new radio telescope, *Atacama Large Millimeter/submillimeter Array* (ALMA) may be able to detect such galaxies at $z \sim 6$ with ~ 2 hours integration, and at $z \sim 8.5$ for ~ 20 hours with 16 antennas (Yajima et al. 2011).

4.4. The Ly α Properties

The resulting Ly α properties of the 60 most massive progenitors from selected snapshots, and their evolution with redshift are shown in Figure 7. The top panel shows the emergent Ly α luminosity $L_{\text{Ly}\alpha}$. The main progenitor has a luminosity of $L_{\text{Ly}\alpha} \sim 10^{42}$ erg s^{-1} at $z \lesssim 2$,

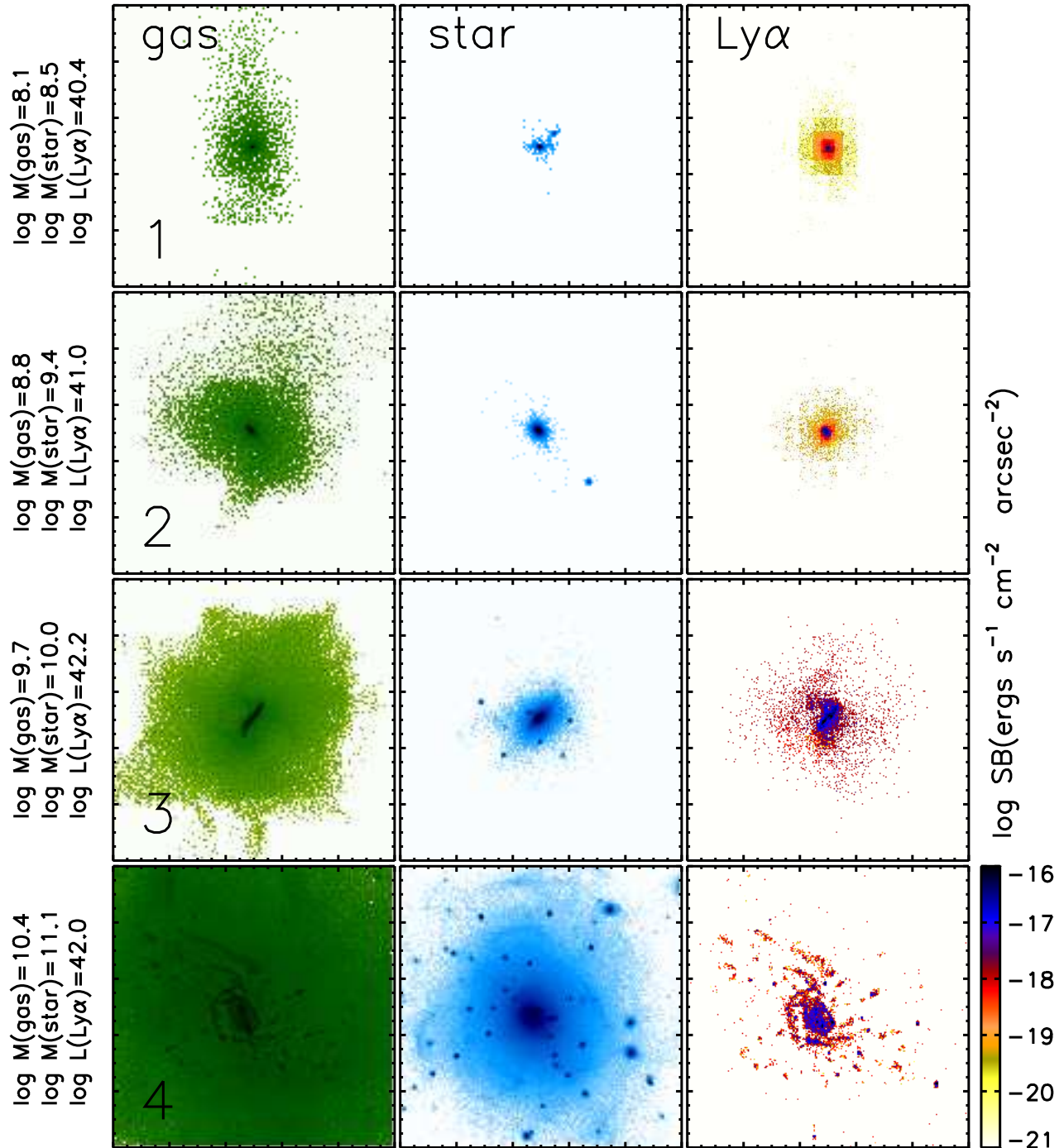


FIG. 5.— The relation between Ly α morphology and galaxy mass, exemplified by a sample of four galaxies at $z = 0.2$ with different masses, $M_{\text{tot}} = 4.2 \times 10^9, 1.7 \times 10^{10}, 1.2 \times 10^{11}$ and $1.6 \times 10^{12} M_{\odot}$, respectively. The left and middle columns show the distribution of gas (in green) and stars (in blue) from the cosmological simulation, respectively. The right column shows the Ly α surface brightness of the corresponding galaxies, with resulting luminosity $L_{\text{Ly}\alpha} = 2.6 \times 10^{40}, 9.8 \times 10^{40}, 1.8 \times 10^{42}$ and 9.8×10^{41} erg s $^{-1}$, respectively. The box size is 250 kpc in physical scale. Note the Ly α luminosity is computed by collecting all escaped photons.

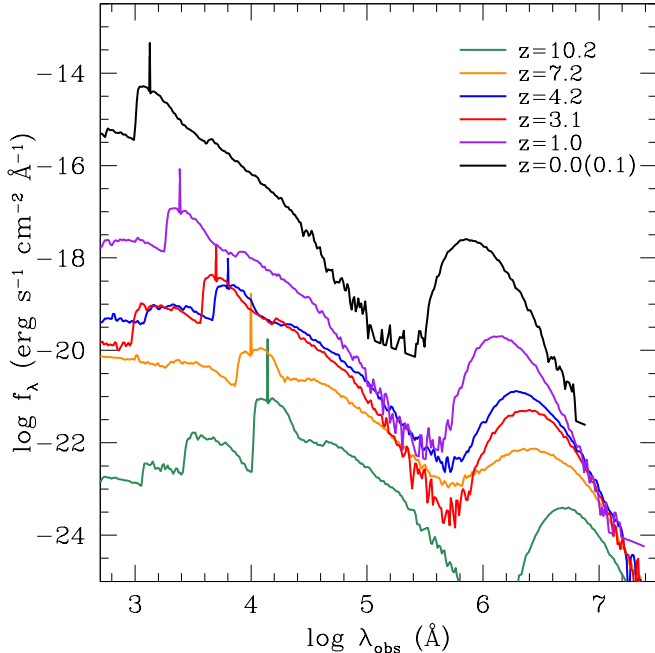


FIG. 6.— The SEDs of the most massive galaxy in each snapshot. Only the galaxy at $z = 0.0$ is artificially set at $z = 0.1$, i.e., the flux is estimated by using the luminosity distance of $z = 0.1$.

then increases to $L_{\text{Ly}\alpha} \sim 10^{43} \text{ erg s}^{-1}$ at $z = 2 - 6$, owing to the increase of SFR. At high redshift $z \gtrsim 6$, the $L_{\text{Ly}\alpha}$ decreases to $\sim 10^{42} \text{ erg s}^{-1}$ due to low escape fraction and absorption by dust. At high redshift, the galaxy size is small and most of the stars form around the galaxy center. Hence, the dust compactly distributes around young stars, which effectively absorbs the ionizing photons. As a result, the intrinsic Ly α emissivity drops even though SFR is enhanced by the accretion of cold gas. However, most of other model galaxies show that the escape fraction of Ly α and UV continuum photons monotonically increases with redshift because of lower dust content. The escaping process of continuum photons will be discussed in detail in a forthcoming paper (Yajima et al. in preparation).

Most of the galaxies at $z \gtrsim 3$ in this simulation have a luminosity below $10^{42} \text{ erg s}^{-1}$, the lower limit of many current observations using narrow-band filters, so they may not be observable. However, the improved sensitivity of deep survey of Cassata et al. (2011) reaches $L_{\text{Ly}\alpha} \sim 10^{41} \text{ erg s}^{-1}$ at $z \sim 2 - 6.6$, which may detect more faint galaxies as the ones in our sample. As mentioned in previous sections, the luminosity is calculated as the sum of all escaped photons. If we consider only pixels brighter than $S = 10^{-18} \text{ ergs s}^{-1} \text{ cm}^{-2} \text{ arcsec}^{-2}$, the detection threshold of high-redshift LAE surveys (e.g., Ouchi et al. 2008, 2010), the total flux of the main progenitor is reduced by a factor of a few, resulting in $L_{\text{Ly}\alpha} \sim 1 - 2 \times 10^{42} \text{ erg s}^{-1}$ in redshift $z \sim 2 - 6$, which is close to the observed $L_{\text{Ly}\alpha}^*$ of LAEs in this redshift span (e.g., Gawiser et al. 2007; Gronwall et al. 2007; Ouchi et al. 2008; Ciardullo et al. 2011). This main progenitor has a halo mass of $\sim 10^{11} M_{\odot}$ at $z \sim 6$, and $\sim 10^{12} M_{\odot}$ at $z \sim 2$, in good agreement with sug-

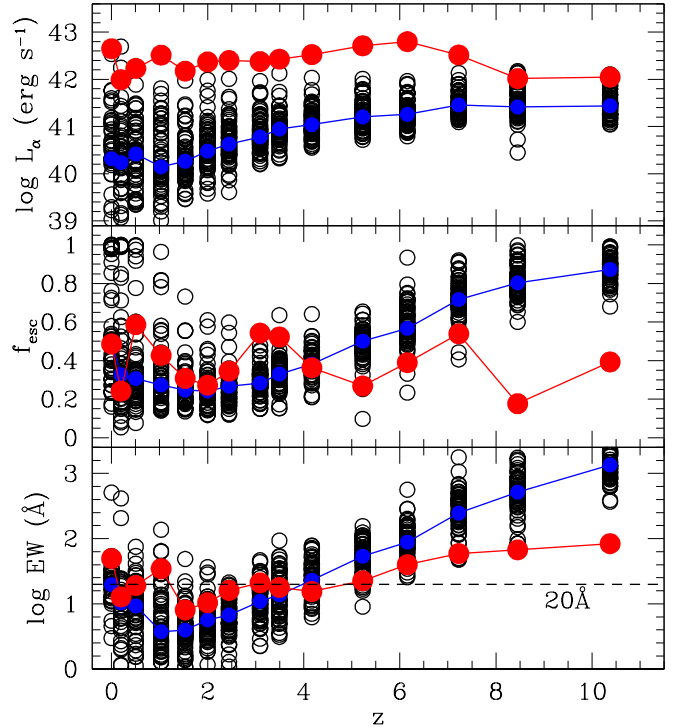


FIG. 7.— Evolution of the Ly α properties of the 60 most massive progenitors from selected redshifts. From top to bottom panel is the emergent unfiltered Ly α luminosity (computed by collecting all escaped photons), escape fraction of Ly α photons over whole solid angle, and equivalent width in rest frame, respectively. The red filled circle represents the value of the main progenitor at each redshift, while the blue filled circles indicate the median value of the sample galaxies.

gestions from clustering analysis by Ouchi et al. (2010). These results suggest that some the observed LAEs at $z \sim 2 - 6$ may be similar to the main progenitors of MW-like L^* galaxies at high redshifts.

The calculated escape fractions of Ly α photons (f_{esc}) are shown in the middle panel of Figure 7. Here, the f_{esc} is estimated by correcting all escaped photons over whole solid angle and dividing by intrinsically emitted photon number. Unlike the SFR, the f_{esc} has higher values at lower redshift $z \lesssim 2$, then decreases gradually to $\sim 20\%$. At $z \gtrsim 4$ the f_{esc} increases again. The f_{esc} of the main progenitor fluctuates in the range of $\sim 20 - 60\%$. The median f_{esc} at $2 \lesssim z \lesssim 4$ is $\sim 30\%$, which is consistent with the recent observation by the HETDEX pilot survey (Blanc et al. 2011). At lower redshift $z \lesssim 1$, there is a large dispersion in f_{esc} , similar to the recent observation by Atek et al. (2009). This large scattering may be caused by variation in a number of physical properties such as SFR, metallicity, and disk orientation. We will discuss the dependence of f_{esc} on these properties in detail in Section 5.1.

We note that the Ly α RT calculations in our work, which take into account local ionization structure and inhomogeneous density distribution of gas and dust, produce a smaller escape fraction ($f_{\text{esc}} \sim 20 - 80\%$ at $z \sim 6$) than that in previous semi-analytical work of Salvadori et al. (2010) ($f_{\text{esc}} \gtrsim 80\%$) and Dayal & Libeskind (2011) ($f_{\text{esc}} \sim 60 - 90\%$), in which

a uniform slab model was assumed. We find that more than half of Ly α photons can be absorbed, because dense gas and dust around the star-forming and Ly α -emitting regions absorb the photons effectively.

The EW of Ly α line is defined by the ratio between the Ly α flux and the UV flux density f_{UV} in rest frame, where the mean flux density of $\lambda = 1300 - 1600 \text{ \AA}$ in rest frame is used. The resulting Ly α EWs are shown in the bottom panel of Figure 7. Most of the galaxies have $EW \gtrsim 20 \text{ \AA}$, they are therefore classified as LAEs (e.g., Gronwall et al. 2007). The median EW increases with redshift, from $\sim 30 \text{ \AA}$ at redshift $z = 0$ to $\sim 820 \text{ \AA}$ at $z \sim 8.5$. This trend is in broad agreement with observations that galaxies at higher redshifts appear to have higher EW than their counterparts at lower redshifts (e.g., Gronwall et al. 2007; Ouchi et al. 2008). The high EW at $z \gtrsim 6$ is produced by excitation cooling, which enhances the Ly α emission at high redshift, but at low redshift it reduces the EW as the stellar population ages (e.g., Finkelstein et al. 2009). Recent observations of LAEs at $z \sim 0.2 - 0.4$ shows that most local LAEs, unlike those at $z \gtrsim 3$, have EWs less than 100 \AA (Deharveng et al. 2008; Cowie et al. 2011), consistent with the trend seen in our model.

We should point out that the results presented in Figure 7 are “unfiltered” by detection limit, and that we caution against taking these numbers too literally when compared with a particular survey, because the observed properties depend strongly on the observational threshold. Note also in the current work, we did not include the transmission in intergalactic medium (IGM). The Ly α properties can be changed by IGM extinction. The neutral hydrogen in IGM at high redshift can scatter a part of Ly α photons, and decrease the $L_{Ly\alpha}$ and EW. For example, Laursen et al. (2011) suggested that the IGM transmission could be $\sim 20 \%$ at $z = 6.5$. The transmission depends sensitively on the viewing angle and the environments of a galaxy, as it is affected by the inhomogeneous filamentary structure of IGM.

4.5. The Ly α Line Profiles

The emergent Ly α emission line of the main progenitor is shown in Figure 8. The frequency of the intrinsic Ly α photon is sampled from a Maxwellian distribution with the gas temperature at the emission location in the rest frame of the gas. Our sample Ly α lines show mostly single peak, common profiles of LAEs observed both at high redshift ($z \sim 6$) (e.g., Ouchi et al. 2010) and in the nearby universe (e.g., Cowie et al. 2010).

In a static and optically thick medium, the Ly α profile can be double peaked, but when the effective optical depth is small due to high relative gas speed or ionization state, there might be only a single peak (Zheng & Miralda-Escudé 2002). In our case, the flow speed of gas is up to $\sim 300 \text{ km/s}$, and the gas is highly ionized by stellar and AGN radiation, which result in a single peak.

In the case at high redshift $z \gtrsim 6$, the gas is highly concentrated around the galaxy center, hence they become optically thick and cause the Ly α photons to move to the wing sides. In addition, the profile at $z = 10.2$ shifts to shorter wavelength, and it shows the characteristic shape of gas inflow (Zheng & Miralda-Escudé 2002). Although

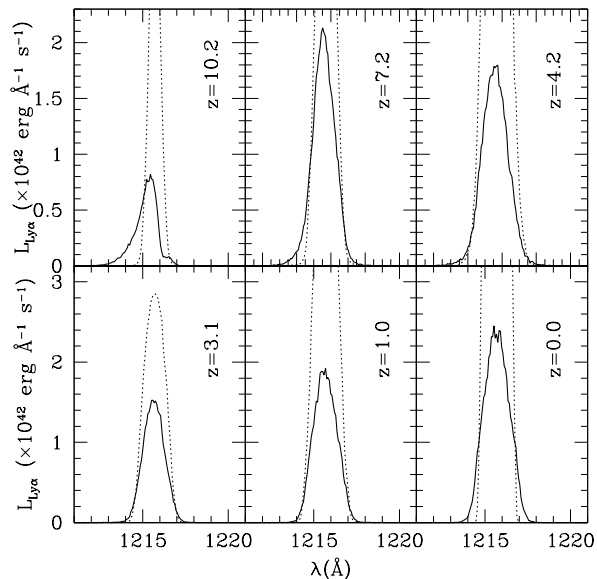


FIG. 8.— The Ly α line profile of the main progenitor at different redshifts. The dotted- and solid lines are the intrinsic and emergent Ly α profile, respectively.

our simulation includes feedback of stellar wind similar to that of Springel et al. (2005b), the Ly α line profile indicates gas inflow in the galaxy. Our result suggests that high-redshift star-forming galaxies may be fueled by efficient inflow of cold gas from the filaments. We will study this phenomenon in detail in Yajima et al. (in preparation). On the other hand, it was suggested that the asymmetrically shifted profile to the red wing in some LAEs can be made by outflowing gas distribution (e.g., Mas-Hesse et al 2003). The growing hot bubble gas around star-forming region from supernovae or radiative feedback can cause outflowing, neutral gas-shells, which result in red-shifted line profiles.

Recently, Yamada et al. (2012) observed a sample of 91 LAEs at $z = 3.1$, about half of which show double peaks of strong-blue and weak-red features thought to be caused by gas outflow, while others show a symmetric single peak in which the flux ratio of blue wing to red one is about unity. While our model may explain the latter, the missing outflow features in our line sample is probably due to the limitations of our current simulations, e.g., insufficient spatial resolution and simplified treatment of supernovae feedback.

In addition, the line profiles of galaxies at high redshift $z \gtrsim 6$ may be highly suppressed and changed by scattering in IGM (e.g., Santos 2004; Dijkstra et al. 2007; Zheng et al. 2010; Laursen et al. 2011), because the Ly α transmission through IGM is very low at the line center and at shorter wavelengths by the Hubble flow (e.g., Laursen et al. 2011). Even at lower redshift $z \sim 3$, the optical depth of IGM can be high depending on the viewing angle and the location of the galaxy (e.g., Laursen et al. 2011). Therefore, the Ly α flux with inflow featured in our model galaxies may be suppressed and the shape may change to a single peak with only the red wing, or a double peak with strong-red and weak-blue as in Figure 7 of Laursen et al. (2011).

5. DISCUSSION

5.1. Dependence of Ly α Properties on Galaxy Properties

As shown in previous Sections, the Ly α properties vary significantly in different galaxies. Here we explore the dependence on a number of physical properties of a galaxy. Figure 9 shows the dependence of escape fraction f_{esc} (top panels) and Ly α luminosity $L_{\text{Ly}\alpha}$ (bottom panels) on the galaxy mass, SFR, and metallicity Z . We apply a least-absolute-deviations fitting to the data using a power-law function, $\log Y = \alpha \log X + \beta$.

The mass dependence of f_{esc} has a large dispersion, but from our fitting, $\alpha \sim -0.02$ and $\beta \sim -0.17$, which suggests that f_{esc} roughly decreases with the total mass, consistent with the results of Laursen et al. (2009). At $M \sim 10^{10-11} M_{\odot}$, the f_{esc} is mostly constant at $\sim 10 - 30$ %. In contrast, f_{esc} is more tightly correlated with the SFR, with $\alpha \sim -0.08$ and $\beta \sim -0.41$. At high SFR, dust can be enriched quickly by type II supernovae, and can effectively absorb the Ly α photons. In addition, galaxies with high SFR have more hydrogen gas. The gas decreases the mean free path of Ly α photons, resulting in the increase of the dust optical depth which reduces the escape fraction. In addition, the f_{esc} decreases with metallicity, $\alpha \sim -0.35$ and $\beta \sim -0.65$. Since the dust content linearly increases with metallicity in our model, the Ly α photons can be absorbed effectively by gas with high metallicity. This trend is consistent with observational indication by Atek et al. (2009) and Hayes et al. (2010).

On the other hand, the luminosity $L_{\text{Ly}\alpha}$ has different relationships with these properties from the f_{esc} . The $L_{\text{Ly}\alpha}$ is also roughly correlated with the mass, $L_{\text{Ly}\alpha} \simeq 10^{37.7} \times M_{\text{tot}}^{0.38}$, with a large dispersion. Only massive galaxies with $M_{\text{tot}} \gtrsim 10^{11} M_{\odot}$ have the Ly α luminosity of $L_{\text{Ly}\alpha} \geq 10^{42} \text{ erg s}^{-1}$. This is consistent with suggestions from clustering analysis of observed LAEs at $z = 2 - 3$ (e.g., Gawiser et al. 2007; Guaita et al. 2010). In our model, the massive galaxies at $z = 2 - 3$ evolve into L^* galaxies at $z = 0$. Hence, our results support the suggestion by Gawiser et al. (2007) that the observed LAEs with $L_{\text{Ly}\alpha} \gtrsim 10^{42} \text{ erg s}^{-1}$ at $z = 2 - 3$ are likely progenitors of local L^* galaxies.

The $L_{\text{Ly}\alpha}$ has the tightest correlation with SFR among the properties investigated here: $L_{\text{Ly}\alpha} \simeq 10^{41.7} \times \text{SFR}^{0.53}$. In the literature, a simple linear relation is commonly used, with $L_{\text{Ly}\alpha} (\text{erg s}^{-1}) = 1.1 \times 10^{42} \times \text{SFR} (M_{\odot} \text{ yr}^{-1})$, assuming that $L_{\text{Ly}\alpha}/L_{\text{H}\alpha} = 8.7$ (case B). However, our result suggests that the relation between $L_{\text{Ly}\alpha}$ and SFR becomes somewhat shallower due to the dependence of f_{esc} on SFR. Finally, the emergent $L_{\text{Ly}\alpha}$ does not show a strong dependence on metallicity, $L_{\text{Ly}\alpha} \simeq 10^{41.1} \times (Z/Z_{\odot})^{-0.27}$. This is due to the fact that, although the intrinsic $L_{\text{Ly}\alpha}$ increases with halo mass (so does SFR and metallicity), the f_{esc} decreases with metallicity, so $L_{\text{Ly}\alpha}$ of higher-metallicity galaxies is suppressed by dust absorption.

We should point out that the large scatter in the correlations in Figure 9 may be due to the small volume of our simulation and the small number of our galaxy sample. In addition, as we discuss in Section 5.6, a number of limitations of our model, such as the simplified ISM

model and insufficient resolutions, may contribute to uncertainty in these relations. Moreover, the luminosity scaling relations may change under some specific detection limits. We will study these relations in detail with improved model and simulations in future work.

5.2. Redshift Dependence of LAE Fraction

The number fraction of LAEs (f_{LAE}) in our sample is shown in figure 10. The detection limit of Ly α varies in different surveys. At high redshifts ($z \gtrsim 3$), the LAE detection in most of observations has been confined to $L_{\text{Ly}\alpha} \gtrsim 10^{42} \text{ erg s}^{-1}$. Here, we derive the f_{LAE} with three $L_{\text{Ly}\alpha}$ thresholds, $L_{\text{Ly}\alpha} \gtrsim 10^{40}, 10^{41}, 10^{42} \text{ erg s}^{-1}$ with EW of $\gtrsim 20 \text{ \AA}$. The f_{LAE} with $L_{\text{Ly}\alpha} \gtrsim 10^{40}, 10^{41} \text{ erg s}^{-1}$ rapidly increases from $z = 0$ to ~ 5 , and then remains nearly constant with higher values $\gtrsim 0.8$ at $z \gtrsim 5$. The trend is roughly similar to the SFR history (Figure 2). Since the $L_{\text{Ly}\alpha}$ is tightly correlated with the SFR (Figure 9), the number of galaxies with $L_{\text{Ly}\alpha} \gtrsim 10^{40}, 10^{41}$ increases at $z \sim 0 - 4$. On the other hand, although the SFR decreases at $z \gtrsim 4$, the f_{esc} increases due to low metallicity. Hence, the f_{LAE} does not decrease at $z \gtrsim 4$.

Meanwhile, the f_{LAE} with $L_{\text{Ly}\alpha} \gtrsim 10^{42} \text{ erg s}^{-1}$ is nearly constant, and shows $\sim 2 - 10$ %. Since the SFR tightly correlates with $L_{\text{Ly}\alpha}$, and it roughly increases with the galaxy mass, some massive galaxies can be LAEs with $L_{\text{Ly}\alpha} \gtrsim 10^{42} \text{ erg s}^{-1}$. In addition, the f_{LAE} of LAEs having intrinsic $L_{\text{Ly}\alpha} \gtrsim 10^{42} \text{ erg s}^{-1}$ change with cosmic star formation history. However, the f_{esc} decreases around the phase of SFR peak, and therefore suppresses the f_{LAE} .

On the other hand, at lower redshift, the observations indicate that number density of LAEs decreases by some factors (e.g., Cowie et al. 2010). The discrepancy may come from the difference in density field and the small box in our simulation. Our initial condition is a somewhat special one which is focused on a MW-size galaxy, and the zoom-in simulation region is $\sim 5^3 h^{-3} \text{ Mpc}^3$. Therefore, our simulation cannot reproduce the global statistics in observations. Moreover, the LAEs fraction having $EW > 25 \text{ \AA}$ in this work shows ~ 44 % at $z=4$ and ~ 100 % at $z = 6$, which is somewhat higher than the LAE fraction in LBG sample (Stark et al. 2010, 2011; Pentericci et al. 2011; Schenker et al. 2012; Ono et al. 2012). However, in observation, the LAE fraction increases with decreasing UV brightness. Most of our model galaxies at $z \gtrsim 3$ are fainter than the detection threshold in the LBG observation. Since the number of galaxies brighter than the threshold of LBG observation is quite small (less than ten), we need a larger sample covering a wide mass range to verify the model of LAEs. In addition, although some LAEs have been observed with UV continuum, and hence categorized as LBGs, it is inadequate to study LAEs from LBG-only sample, because a large fraction of LAEs may have UV continuum under the detection limit of current observations. We will address the general properties such as luminosity function, EW distribution and clustering systematically by using a set of uniform simulations with mean density field in larger volumes in future work.

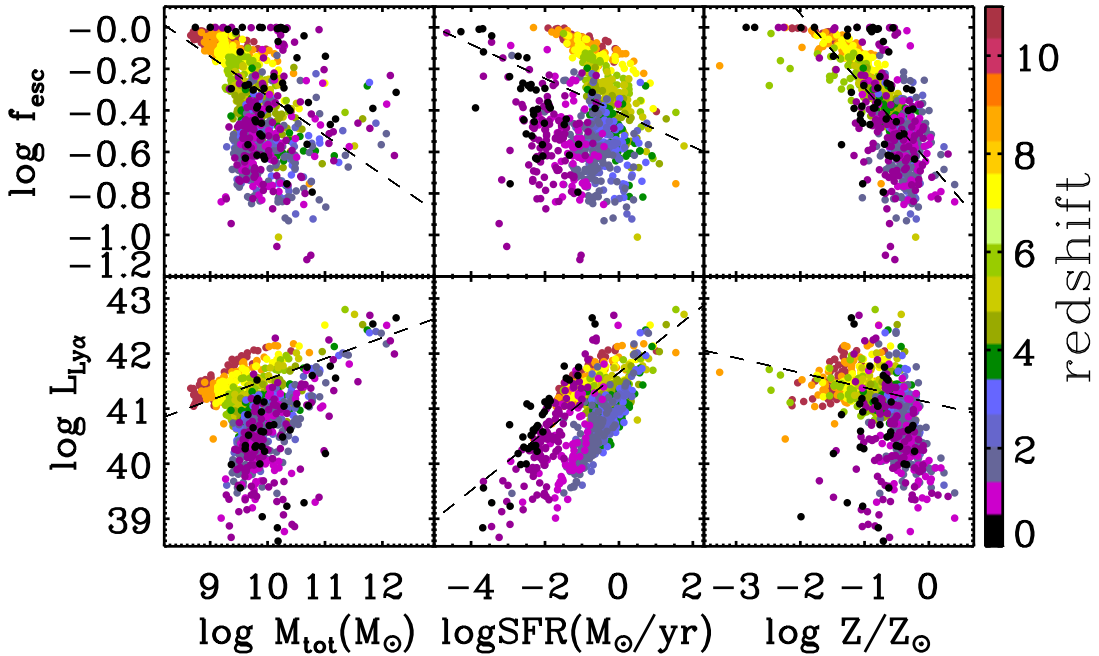


FIG. 9.— Dependence of Ly α properties on various physical properties of a galaxy. Upper : The relation between Ly α escape fraction and halo mass, SFR and metallicity. The different color represents the different redshift, as indicated in the color bar. The dash lines are least-absolute-deviations fittings. Lower : The relation between Ly α luminosity and halo mass, SFR and metallicity.

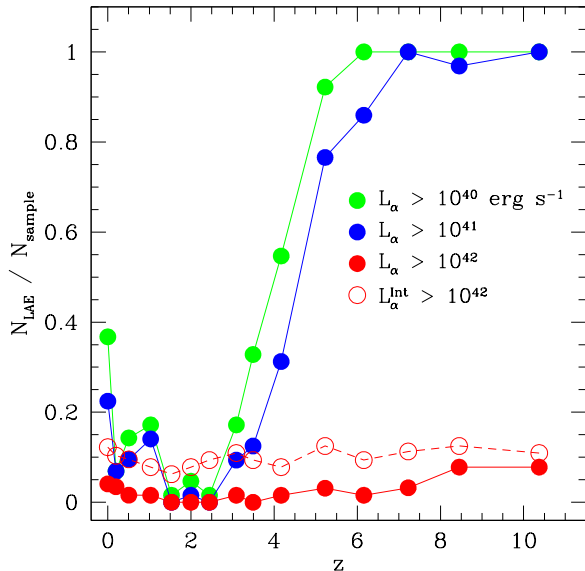


FIG. 10.— Number fraction of LAEs in our galaxy sample. The green, blue and red filled circles represent the fraction at Ly α luminosity threshold, 10^{40} , 10^{41} , and 10^{42} erg s $^{-1}$, respectively.

5.3. The Viewing-angle Scatter of Escaping Ly α Photons

Despite their high metallicity, a fraction of galaxies at low redshift $z \lesssim 1$ show high escape fraction f_{esc} of Ly α photons (Figure 9). We find that the escaping angle of the Ly α photons depends strongly on the galaxy morphology and orientation, a phenomenon we dub as the “viewing-angle scatter”. Disky objects seen edge on can be hundred times fainter than the same objects seen face on. In a galaxy which has a gas disk, the Ly α photons

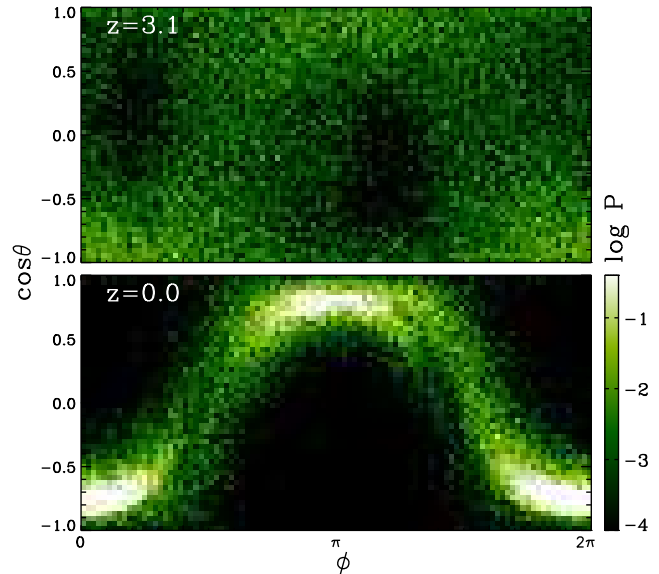


FIG. 11.— The “viewing-angle scatter” of escaping Ly α photons depends strongly on galaxy morphology and orientation. Shown here is the Ly α escape probability in an irregular galaxy progenitor at $z=3.1$ (top panel) and the spiral MW galaxy at $z=0$ (bottom panel). The color bar indicates the probability per unit $d\phi, d\cos\theta$. There is no clear direction in the irregular galaxy, but in the disk galaxy, the Ly α photons escape in a preferred direction normal to the disk.

escape in a preferred direction normal to the disk, but there is no clear escaping direction in compact or irregular galaxies without a gas disk. We demonstrate this effect in Figure 11. We first estimate the normal direc-

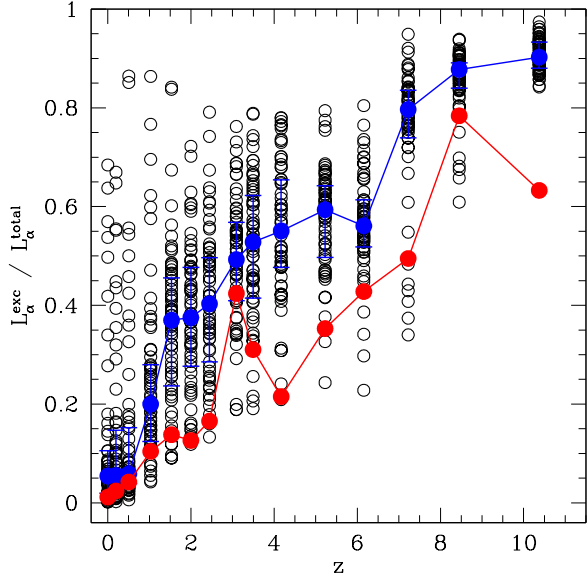


FIG. 12.— The fraction of excitation cooling Ly α to the total intrinsic Ly α luminosity as a function of redshift. The red filled circles indicate the values of the main progenitor, while the blue filled circles represent the median value of the galaxy sample indicated with black open circles. The error bars show the quartiles.

tion to the gas disk according to the total angular momentum of the gas, and set $\theta = 0^\circ$ along this direction. In a galaxy with irregular morphology such as the main progenitor at $z = 3.1$, there is no clear preferred escaping angle, as illustrated in the top panel of Figure 11. However, in a spiral galaxy with rotationally supported gas disk such as the MW galaxy at $z=0$ in our simulation, the escaping angle is strongly confined to $\cos\theta \simeq \pm 1$, corresponding to $\theta \simeq 0^\circ$ or 180° , as shown in the bottom panel of Figure 11. This is due to the fact that the Ly α photons have the minimum optical depth along the normal direction to the gas disk. More than 60 % Ly α photons escapes to the direction of $|\cos\theta| \gtrsim 0.5$. Generally the Ly α flux from our model galaxies can scatter around the mean value typically by a factor of ten just from different orientations.

As illustrated in Figure 3, most galaxies in our simulation have highly irregular shapes at high redshift due to accretion and gravitational interaction. At $z=0$, a number of them evolve into spiral disks. The “viewing-angle scatter” explains why we see high Ly α escape fractions in a number of low- z galaxies, and the fact that Ly α is detected in a large number of face-on spiral galaxies in the nearby universe (e.g., Cowie et al. 2010).

5.4. Contribution of Excitation Ly α Cooling

There are two major mechanisms to generate Ly α emission, the recombination of ionizing photons and the collisional excitation of hydrogen gas. However, the relative contribution between the two mechanisms is not well understood. From our calculations, we find that the contributing fraction of excitation Ly α emission to the total intrinsic Ly α luminosity increases with redshift, as shown in figure 12.

In our cosmological simulation, galaxy evolution is accompanied by cold, filamentary gas streams with tem-

perature $T \sim 10^{4-5}$ K, which penetrate deep inside dark matter halos (Zhu et al. in preparation, Yajima et al. in preparation), a phenomenon also reported by other groups (Katz et al. 2003; Kereš et al. 2005, 2009; Birnboim & Dekel 2003; Dekel & Birnboim 2006; Ocvirk et al. 2008; Brooks et al. 2009; Dekel et al. 2009). Such cold gas can efficiently produce the excitation Ly α cooling photons (Dijkstra & Loeb 2009; Faucher-Giguère et al. 2009; Goerdt et al. 2010). At higher redshift, galaxies form through more efficient gas accretion and more frequent merging event. As a result, the contributing fraction increases with redshift, and becomes dominant at $z \gtrsim 6$. This excitation mechanism does not depend on the stellar radiation, and can therefore produce high Ly α EWs. We find that the EWs of LAEs increases significantly at $z \gtrsim 6$, reaching $\gtrsim 10^3$ Å at $z \sim 10$. This is larger than the upper-limit of EW, 240 Å, which considers only stellar sources assuming a Salpeter IMF with solar abundance of metallicity (Charlot & Fall 1993). Although the upper-limit increases with decreasing metallicity, it was suggested that top-heavy IMF like Pop III stars are needed for making $\text{EW} > 400$ Å (Schaerer 2003; Raiter et al. 2010). However, even though Salpeter-IMF is used in this work and the stellar metallicity is mostly $Z/Z_\odot \gtrsim 10^{-3}$, we find that the EW can be higher than the upper-limit by the efficient excitation Ly α emission. On the other hand, the Ly α line is strongly damped by IGM correction at $z \gtrsim 6$ (Haiman 2002; Laursen et al. 2011; Dayal & Libeskind 2011), which can result in a lower EW. The suppression by IGM highly depends on the inhomogeneous ionization structure around LAEs (e.g., McQuinn et al. 2007; Mesinger & Furlanetto 2008; Iliev et al. 2008). We will address the detectability of high-redshift LAEs and EW after IGM correction by running large-scale Ly α RT in IGM in future work.

5.5. Ly α Luminosity Functions

The simulation box in this work is too small to study global statistics directly. As a rough estimate, we use the luminosity – halo mass correlation we find above may be used to construct Ly α luminosity functions (LFs) at different redshift when combined with halo mass functions from large-box, general cosmological simulations. For example, at $z = 3.1$, we divide all galaxies in the snap shot by the halo mass with 0.25 dex, and fit to the median value of each bin, this gives a correlation of $L_{\text{Ly}\alpha} (\text{erg s}^{-1}) = 10^{32.94} \times (M_{\text{halo}}^{0.79}/M_\odot)$. We then use this to convert the halo mass function of Sheth & Tormen (1999) to the Ly α LF.

Figure 13 shows the resulting Ly α LFs in comparison with observations at redshift $z = 3.1, 5.7$, respectively. The red solid curves are LFs above a detection threshold of $S_{\text{Ly}\alpha} = 10^{-18} \text{ ergs s}^{-1} \text{ cm}^{-2} \text{ arcsec}^{-2}$ (Ouchi et al. 2008, 2010), while the red dashed lines represent LFs from total luminosity (counting all escaped photons without a flux cut).

While the un-filtered LFs seem to agree with observations of Gronwall et al. (2007) and Ouchi et al. (2008), the filtered ones are significantly off. The difference comes from the reduction of $L_{\text{Ly}\alpha}$ and f_{esc} due to the flux cut. Moreover, the dispersion in the luminosity – halo mass relation at different redshift may cause a large

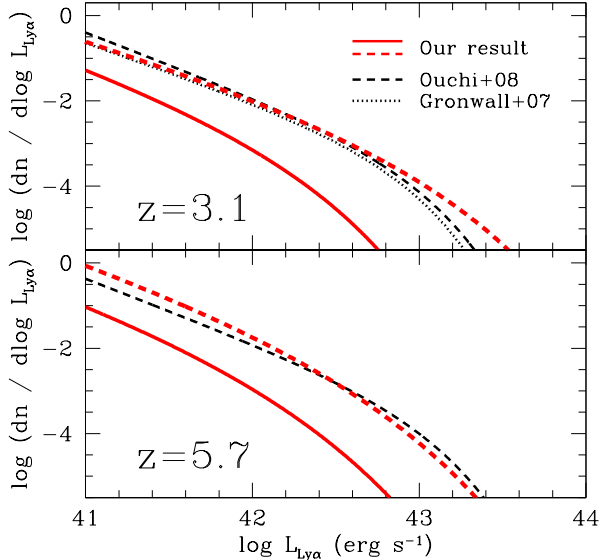


FIG. 13.— Derived Ly α luminosity functions from our model in comparison with observations. The red, solid lines are filtered LFs above a detection threshold of $S_{\text{Ly}\alpha} = 10^{-18} \text{ ergs s}^{-1} \text{ cm}^{-2} \text{ arcsec}^{-2}$ (Ouchi et al. 2008), while the red, dashed lines represent unfiltered ones. The black dashed lines are the Schechter function at $z = 3.1$ and 5.7 derived from LAEs observation by Ouchi et al. (2008), and the black dotted line is from observation at $z = 3.1$ by Gronwall et al. (2007).

scatter in the LFs. This plot suggests that the current simulation in this work is not suitable to study a large galaxy population and its statistical properties, because there are too few observable LAEs. Moreover, as discussed earlier, the predicted Ly α properties may be affected by a number of numerical and physical limitations of our model. For example, the one-phase model currently used in the present work may underestimate the density of cold hydrogen gas, and hence underestimates the Ly α flux. We will study the Ly α LFs at different redshift in a forthcoming paper with the improved ART² which incorporates a two-phase ISM model, and a general simulation with mean overdensity in a larger volume (Yajima et al, in preparation).

5.6. Limitations of Our Model

As demonstrated above, our model is able to explain a number of observed properties of LAEs at different redshift. However, we should point out that our current simulations suffer from a number of major limitations which may affect the predicted Ly α properties.

- In the current work, we use a one-phase ISM model, which considers the average density and temperature of the gas. Such a model likely underestimates the density of cold hydrogen gas, which may lead to significant underestimate of the Ly α emission coming from cold ($\sim 10^4$ K), dense gas. On the other hand, such a model also underestimates the amount of dust associated with cold molecular gas, which likely results in underestimate of absorption of Ly α photons by gas and dust. We will investigate the Ly α RT and ionization structures in a two-phase ISM model in a forthcoming paper.

- The absorption and transmission of IGM are not taken into account in the RT calculations. As discussed in the previous section, these two effects may suppress the Ly α flux and change the line profiles.
- The simulations do not have sufficient resolutions to resolve dense regions and outflow, which requires a high spatial resolution of $\sim \text{pc}$ (e.g., Fujita et al. 2009). It is a challenge for cosmological simulations to resolve both the inflow gas from large scales of $\sim \text{Mpc}$ and the outflow from pc-scale star forming regions. For a simulation with a box of 100 Mpc like the one we have, this requires a large dynamical range over eight orders of magnitude, which is beyond the scope of our current work.
- The simulation box in this work is too small to study a large galaxy population, as well as effects of environment on galaxy properties and their evolution. One needs uniform simulations in large volumes in order to systematically investigate the formation and evolution of L^* galaxies.

Finally, we stress once again that caution should be taken when comparing directly the results from our calculations to data from a given survey, because, as discussed above, the observed Ly α properties depend sensitively on a number of factors, including galaxy properties, viewing angle, model parameters, and observational threshold.

6. SUMMARY

To summarize, we have investigated the Ly α properties of progenitors of a local L^* galaxy by combining cosmological hydrodynamic simulations with three-dimensional radiative transfer calculations using the new ART² code. Our cosmological simulation follows the formation and evolution of a Milky Way-size galaxy and its substructures from redshift $z = 127$ to $z = 0$. It includes important physics of dark matter, gas dynamics, star formation, black hole growth, and feedback processes, and has high spatial and mass resolutions to resolve a MW-like galaxy at $z=0$ and its progenitors at higher redshifts. Our radiative transfer couples Ly α line, ionization of neutral hydrogen, and multi-wavelength continuum radiative transfer, which enables a self-consistent and accurate calculation of the Ly α properties in galaxies.

We find that the main progenitor of the MW galaxy is Ly α bright at high redshift, with the emergent Ly α luminosity close to the observed characteristic $L_{\text{Ly}\alpha}^*$ of LAEs at $z \sim 2 - 6$. Most of the fainter galaxies in the simulation fall below the detection threshold of many current surveys. The Ly α escape fraction correlates with a number of physical properties of the galaxy, such as mass, SFR and metallicity. We find a “viewing-angle scatter” in which the photon escape depends strongly on the galaxy morphology and orientation, such that the Ly α photons escape in a preferred direction normal to the gas disk in disk galaxies, but randomly in compact or irregular galaxies. Moreover, the EWs of LAEs increases with redshift, from tens of Angstroms at redshift $z \sim 0$ to hundreds of Angstroms at $z \sim 8.5$. Furthermore, we find that high-redshift LAEs show Ly α line profiles

characteristic of gas inflow, and that the Ly α emission by excitation cooling increases with redshift, accounting $\sim 50\%$ of the total at $z \gtrsim 6$.

Our results suggest that galaxies at high redshift form through accretion of cold gas, which accounts for the the high EWs, the blue-shifted line profiles, and the dominant contribution from excitation cooling in Ly α emission. Moreover, some of the observed LAEs at $z \sim 2 - 6$ with $L_{\text{Ly}\alpha} \sim 10^{42-43} \text{ erg s}^{-1}$ may evolve into present-day L^* galaxies such as the Milky Way.

We thank Carlos Frenk for kindly providing us the Aquila initial condition for the cosmological simulation. We thank Mark Dijkstra, Claude-André Faucher-Giguère, Eric Gawiser, Lars Hernquist, and Avi Loeb for stimulating discussions and helpful comments, as well as

the referee for an insightful report which has helped improve the manuscript. Support from NSF grants AST-0965694 & AST-1009867 (to YL), AST-0807075 (to TA), and AST-0807885 (to CG & RC) is gratefully acknowledged. YL thanks the Institute for Theory and Computation (ITC) at Harvard University where the project was started for warm hospitality. We acknowledge the Research Computing and Cyberinfrastructure unit of Information Technology Services at The Pennsylvania State University for providing computational resources and services that have contributed to the research results reported in this paper (URL: <http://rcc.its.psu.edu>). The Institute for Gravitation and the Cosmos is supported by the Eberly College of Science and the Office of the Senior Vice President for Research at the Pennsylvania State University.

REFERENCES

- Acquaviva, V., Vargas, C., Gawiser, E., & Guaita, L. 2011, arXiv:1111.6688
- Atek, H., et al. 2009, *A&A*, 506, L1
- Barnes, J., & Hut, P. 1986, *Nature*, 324, 446
- Birnboim, Y., & Dekel, A. 2003, *MNRAS*, 345, 349
- Blanc, et al. 2011, *ApJ*, 736, 31
- Bond, N., et al. 2011, ArXiv e-prints
- Bondi, H. 1952, *MNRAS*, 112, 195
- Bondi, H., & Hoyle, F. 1944, *MNRAS*, 104, 273
- Bongiovanni, A., et al. 2010, *A&A*, 519, L4+
- Brooks, A. M., Governato, F., Quinn, T., Brook, C. B., & Wadsley, J. 2009, *ApJ*, 694, 396
- Bruzual, G., & Charlot, S. 2003, *MNRAS*, 344, 1000
- Cassata, P., et al. 2011, *A&A*, 525, 143
- Charlot, S., & Fall, S. M. 1993, *ApJ*, 415, 580
- Ciardullo, R., et al. 2011, ArXiv e-prints
- Cowie, L. L., Barger, A. J., & Hu, E. M. 2010, *ApJ*, 711, 928
- . 2011, *ApJ*, 738, 136
- Cowie, L. L., & Hu, E. M. 1998, *AJ*, 115, 1319
- Cuby, J.-G., et al. 2007, *A&A*, 461, 911
- Davé, R., Hernquist, L., Katz, N., & Weinberg, D. H. 1999, *ApJ*, 511, 521
- Dawson, S., et al. 2004, *ApJ*, 617, 707
- Dayal, P., & Libeskind, N. I. 2012, *MNRAS*, 419, L9
- Dayal, P., Ferrara, A., & Gallerani, S. 2008, *MNRAS*, 389, 1683
- Dayal, P., Maselli, A., & Ferrara, A. 2011, *MNRAS*, 410, 830
- Deharveng, J.-M., et al. 2008, *ApJ*, 680, 1072
- Dekel, A., & Birnboim, Y. 2006, *MNRAS*, 368, 2
- Dekel, A., et al. 2009, *Nature*, 457, 451
- Di Matteo, T., Colberg, J., Springel, V., Hernquist, L., & Sijacki, D. 2008, *ApJ*, 676, 33
- Di Matteo, T., Springel, V., & Hernquist, L. 2005, *Nature*, 433, 604
- Dijkstra, M., Lidz, A., & Wyithe, J. S. B. 2007, *MNRAS*, 377, 1175
- Dijkstra, M., & Loeb, A. 2009, *MNRAS*, 400, 1109
- Faucher-Giguère, C., Lidz, A., Zaldarriaga, M., & Hernquist, L. 2009, *ApJ*, 703, 1416
- Finkelstein, S. L., Cohen, S. H., Malhotra, S., & Rhoads, J. E. 2009, *ApJ*, 700, 276
- Finkelstein, S. L., et al. 2011, *ApJ*, 729, 140
- Fujita, A., Martin, C. L., Mac Low, M.-M., New, K. C. B., & Weaver, R. 2009, *ApJ*, 698, 693
- Fynbo, J. P. U., Ledoux, C., Möller, P., Thomsen, B., & Burud, I. 2003, *A&A*, 407, 147
- Fynbo, J. U., Möller, P., & Thomsen, B. 2001, *A&A*, 374, 443
- Gawiser, E., et al. 2007, *ApJ*, 671, 278
- Gawiser, E., et al. 2006, *ApJ*, 642, L13
- Goerdt, T., et al. 2010, *MNRAS*, 407, 613
- Gronwall, C., et al. 2007, *ApJ*, 667, 79
- Guaita, L., et al. 2010, *ApJ*, 714, 255
- Haardt, F., & Madau, P. 1996, *ApJ*, 461, 20
- Haiman, Z. 2002, *ApJ*, 576, L1
- Hayes, M., et al. 2007, *MNRAS*, 382, 1465
- Hayes, M., et al. 2010, *Nature*, 464, 562
- Hayes, M., et al. 2011, *ApJ*, 730, 8
- Hernquist, L., & Katz, N. 1989, *ApJS*, 70, 419
- Hockney, R. W., & Eastwood, J. W. 1981, *Computer Simulation Using Particles*, ed. Hockney, R. W. & Eastwood, J. W., Computer Simulation Using Particles
- Hopkins, A. M., & Beacom, J. F. 2006, *ApJ*, 651, 142
- Hopkins, P. F., et al. 2006, *ApJS*, 163, 1
- Horton, A., Parry, I., Bland-Hawthorn, J., Cianci, S., King, D., McMahon, R., & Medlen, S. 2004, in *Society of Photo-Optical Instrumentation Engineers (SPIE) Conference Series*, Vol. 5492, Society of Photo-Optical Instrumentation Engineers (SPIE) Conference Series, ed. A. F. M. Moorwood & M. Iye, 1022–1032
- Hoyle, F., & Lyttleton, R. A. 1941, *MNRAS*, 101, 227
- Hu, E. M., & Cowie, L. L. 2006, *Nature*, 440, 1145
- Hu, E. M., et al. 2010, *ApJ*, 725, 394
- Hu, E. M., et al. 2004, *AJ*, 127, 563
- Hu, E. M., Cowie, L. L., & McMahon, R. G. 1998, *ApJ*, 502, L99
- Hu, E. M., et al. 2002, *ApJ*, 568, L75
- Hu, E. M., & McMahon, R. G. 1996, *Nature*, 382, 231
- Hui, L., & Gnedin, N. Y. 1997, *MNRAS*, 292, 27
- Iliev, I. T., Shapiro, P. R., McDonald, P., Mellema, G., & Pen, U.-L. 2008, *MNRAS*, 391, 63
- Iye, M., et al. 2006, *Nature*, 443, 186
- Kashikawa, N., et al. 2006, *ApJ*, 648, 7
- Katz, N., Keres, D., Dave, R., & Weinberg, D. H. 2003, in *Astrophysics and Space Science Library*, Vol. 281, The IGM/Galaxy Connection. The Distribution of Baryons at $z=0$, ed. J. L. Rosenberg & M. E. Putman, 185–
- Katz, N., Weinberg, D. H., Hernquist, L., & Miralda-Escude, J. 1996, *ApJ*, 457, L57
- Keel, W. C., White, III, R. E., Chapman, S., & Windhorst, R. A. 2009, *ApJ*, 138, 986
- Kennicutt, Jr., R. C. 1998, *ARA&A*, 36, 189
- Kereš, D., Katz, N., Fardal, M., Davé, R., & Weinberg, D. H. 2009, *MNRAS*, 395, 160
- Kereš, D., Katz, N., Weinberg, D. H., & Davé, R. 2005, *MNRAS*, 363, 2
- Kodaira, K., et al. 2003, *PASJ*, 55, L17
- Komatsu, E., et al. 2009, *ApJS*, 180, 330
- Lai, K., et al. 2007, *ApJ*, 655, 704
- Lai, K., et al. 2008, *ApJ*, 674, 70
- Laursen, P., Sommer-Larsen, J., & Andersen, A. C. 2009, *ApJ*, 704, 1640
- Laursen, P., Sommer-Larsen, J., & Razoumov, A. O. 2011, *ApJ*, 728, 52
- Lehnert, M. D., et al. 2010, *Nature*, 467, 940
- Li, Y., et al. 2007, *ApJ*, 665, 187
- Li, Y., et al. 2008, *ApJ*, 678, 41
- Maier, C., et al. 2003, *A&A*, 402, 79
- Malhotra, S., & Rhoads, J. E. 2004, *ApJ*, 617, L5
- Malhotra, S., et al. 2011, arXiv:1106.2816
- Mas-Hesse, J. M., Kunth, D., Tenorio-Tagle, G., Leitherer, C., Terlevich, R. J., & Terlevich, E. 2003, *ApJ*, 598, 858

- Matsuda, Y., et al. 2011, MNRAS, 410, L13
 Mesinger, A., & Furlanetto, S. R. 2008, MNRAS, 386, 1990
 McQuinn, M., Hernquist, L., Zaldarriaga, M., & Dutta, S. 2007, MNRAS, 381, 75
 Nilsson, K. K., & Møller, P. 2011, A&A, 527, L7
 Nilsson, K. K., et al. 2007, A&A, 471, 71
 Nilsson, K. K., et al. 2011, A&A, 529, A9
 Nilsson, K. K., et al. 2009, A&A, 498, 13
 Ocvirk, P., Pichon, C., & Teyssier, R. 2008, MNRAS, 390, 1326
 Ono, Y., et al. 2010a, MNRAS, 402, 1580
 Ono, Y., et al. 2010b, ApJ, 724, 1524
 Ono, Y., et al. 2012, ApJ, 744, 83
 Osterbrock, D. E., & Ferland, G. J. 2006, Astrophysics of gaseous nebulae and active galactic nuclei, ed. Osterbrock, D. E., & Ferland, G. J., Astrophysics of gaseous nebulae and active galactic nuclei
 Östlin, G., et al. 2009, AJ, 138, 923
 Ota, K., et al. 2008, ApJ, 677, 12
 Ouchi, M., et al. 2008, ApJS, 176, 301
 Ouchi, M., et al. 2003, ApJ, 582, 60
 Ouchi, M., et al. 2010, ApJ, 723, 869
 Partridge, R. B. & Peebles, P. J. E. 1967, ApJ, 147, 868
 Pentericci, L., et al. 2009, A&A, 494, 553
 Pentericci, L., et al. 2011, ApJ, 743, 132
 Pirzkal, N., Malhotra, S., Rhoads, J. E., & Xu, C. 2007, ApJ, 667, 49
 Raiter, A., Schaerer, D., & Fosbury, R. A. E. 2010, A&A, 523, 64
 Rhoads, J. E., et al. 2003, AJ, 125, 1006
 Rhoads, J. E., et al. 2000, ApJ, 545, L85
 Salpeter, E. E. 1955, ApJ, 121, 161
 Salvadori, S., Dayal, P., & Ferrara, A. 2010, MNRAS, 407, L1
 Santos, M. R. 2004, MNRAS, 349, 1137
 Schaerer, D. 2003, A&A, 397, 527
 Schenker, M. A., et al. 2012, ApJ, 744, 179
 Schmidt, M. 1959, ApJ, 129, 243
 Sheth, R. K., & Tormen, G. 1999, MNRAS, 308, 119
 Shimasaku, K., et al. 2006, PASJ, 58, 313
 Springel, V. 2005, MNRAS, 364, 1105
 Springel, V., Di Matteo, T., & Hernquist, L. 2005a, ApJL, 620, L79
 —. 2005b, MNRAS, 361, 776
 Springel, V., & Hernquist, L. 2002, MNRAS, 333, 649
 —. 2003, MNRAS, 339, 289
 Springel, V., et al. 2008, MNRAS, 391, 1685
 Springel, V., Yoshida, N., & White, S. D. M. 2001, New Astronomy, 6, 79
 Stark, D. P., et al. 2007, ApJ, 663, 10
 Stark, D. P., Ellis, R. S., Chiu, K., Ouchi, M. & Bunker, A. 2010, MNRAS, 408, 1628
 Stark, D. P., Ellis, R. S., & Ouchi, M. 2011, ApJ, 728, L2
 Steidel, C. C., et al. 2000, ApJ, 532, 170
 Stern, D., et al. 2005, ApJ, 619, 12
 Taniguchi, Y., et al. 2005, PASJ, 57, 165
 Vanzella, E., et al. 2011, ApJ, 730, L35
 Wadepuhl, M., & Springel, V. 2011, MNRAS, 410, 1975
 Willis, J. P., Courbin, F., Kneib, J.-P., & Minniti, D. 2008, MNRAS, 384, 1039
 Xu, G. 1995, ApJS, 98, 355
 Yajima, H., Li, Y., Zhu, Q., & Abel, T. 2011, arXiv: 1109.4891
 Yamada, T., et al. 2012, arXiv: 1203.3633
 Zheng, Z., Cen, R., Trac, H., & Miralda-Escudé, J. 2010, ApJ, 716, 574
 Zheng, Z. & Miralda-Escudé, J. 2002, ApJ, 578, 33